



# Effects of Turbulence Models on Flow Characteristics of a Vertical Fire Pump

F. K. Osman<sup>1</sup>, J. Zhang<sup>1†</sup>, L. Lai<sup>1</sup> and A. A. Kwarteng<sup>2</sup>

<sup>1</sup> National Research Center of Pumps, Jiangsu University, Zhenjiang, 212013, China

<sup>2</sup> Department of Mechanical Engineering, University of Mines and Technology, Tarkwa, Ghana

†Corresponding Author Email: [zhangjinfeng@ujs.edu.cn](mailto:zhangjinfeng@ujs.edu.cn)

(Received May 12, 2022; accepted July 30, 2022)

## ABSTRACT

The flow in the vertical long-axis fire pump exhibits complex, three-dimensional, unsteady flow features. In an attempt to understand the effects of turbulence models on the flow mechanism and performance characteristics of the pump, the ANSYS CFX software was used to carry out numerical studies on the vertical fire pump using URANS. The main objective of this study was to investigate the unsteady flow dynamics within the vertical fire pump and the influence of applying different computational turbulence models. The study then sought to conduct a brief analysis of the unsteady pressure pulsation characteristics of the pump. The reliability of the CFD model was validated with an external characteristic test. The transient pressure distribution, velocity field and external characteristics were analyzed. The results were compared to experimental results, where it was revealed that the SST  $k-\omega$  model showed 1.82% and 0.81% improvements in efficiency and head, respectively, over the  $k-\epsilon$  models. In terms of the power performance, however, the standard  $k-\epsilon$  is less likely to over-predict the power used by the pump in overload conditions as compared to the other turbulence models. The pressure charts did not show significant reactions to varying turbulence models across all the studied flow rates. However, the velocity streamlines revealed that there were several disruptions in streamwise flow, where both the standard and RNG  $k-\epsilon$  models exhibited more recirculation areas than the SST  $k-\omega$  and standard  $k-\omega$  models. Overall, for this type of application, SST  $k-\omega$  was the best-performing turbulence model, while RNG  $k-\epsilon$  showed the poorest performance. Nonetheless, the RNG  $k-\epsilon$  also has its strengths. This investigation would serve as a theoretical reference for further research and development in fluid machinery.

**Keywords:** Vertical fire pump; Numerical simulation; CFD; Turbulence model; SST  $k-\omega$ .

## NOMENCLATURE

$C_p$	pressure coefficient	$\rho$	density
$C_\mu$	constant	$\bar{p}$	mean pressure
$g$	gravity	$\eta$	efficiency
$H$	head	$\omega$	angular speed
$k$	kinetic energy of turbulence	$\omega$	specific dissipation of turbulence kinetic energy
$n$	rotational speed	$u_i, u_j$	time averaged velocity components
$P$	pressure	$-\rho \overline{u'_i u'_j}$	Reynolds stress tensor
$P_i$	instantaneous pressure	$\mu_t$	turbulent viscosity
$Q$	flow rate	$\delta_{ij}$	Kronecker delta
$Q_d$	design flow rate		
$t$	time		
$\epsilon$	dissipation of kinetic energy of turbulence		

### Abbreviations

CFD	Computational Fluid Dynamics
URANS	Unsteady Reynolds-Averaged Navier–Stokes
SST	Shear Stress Transport
RNG	Renormalization Group

### Subscripts

$i, j$	components in different directions
$x_i$	Cartesian coordinates: $x, y, z$

TKE      Turbulent Kinetic Energy  
 BPF      Blade Passing Frequency

## 1. INTRODUCTION

Vertical fire pumps are characterized by large flow rates and high heads, as well as the advantages of quick start-up times, higher structural integrity, and broad applicability in a variety of situations. Therefore, they are frequently employed for projects such as offshore platforms, urban drainage and storm water management, feedwater supply, and a variety of other applications. This increased desire for vertical long-axis fire pumps also results in higher expectations for their performance (Hu *et al.* 2012; Yu 2014; Zhang *et al.* 2021).

Given its high precision, Computational Fluid Dynamics (CFD) is frequently used in the pump industry to analyze their flow characteristics for performance improvement (Wang *et al.* 2021; Zhang *et al.* 2019). Accurate turbulence modeling is required to be able to correctly predict the effects of turbulence. Several researchers have conducted investigations over the years (Menter and Egorov 2010, 2006; Menter 1992, 1994, 2009; Opoku *et al.* 2020; Uddin *et al.* 2020). In fluid machinery systems, there have been several studies on the influence of turbulence models in identifying the onset, source, and development of flow instabilities (Asuaje *et al.* 2005; Deniz *et al.* 2019; Nikou and Ehsani 2008).

Feng *et al.* (2010) carried out a study in which several turbulence models were used to analyze the fluid flow at  $1.0Q_d$  and  $0.5Q_d$  flow conditions. A comparison of turbulence models in stirred tanks by the use of different types of impellers was conducted by Joshi *et al.* (2011). They concluded that the  $k-\epsilon$  turbulence model struggled in the task of accurately predicting the mean flow characteristics. In addition, it could not predict some turbulent kinetic energy contours in the impeller domain. Chalhoun *et al.* (2016) used three turbulence models to numerically investigate the flow domain within a centrifugal pump and found that, at design flow conditions, the SST  $k-\omega$  model accurately predicted the pump's performance when compared to the other models. Al-Obaidi (2019) used the behavior of turbulence models to forecast the likelihood of cavitation in a centrifugal pump and concluded that the type of turbulence model used plays a substantial role in cavitation prediction.

Choosing the appropriate turbulence model for CFD analysis in a pump, on the other hand, is always a challenge. The flow of a vertical fire pump was studied using CFD with several turbulence models under design and off-design settings in this paper. The off-design conditions were selected in accordance with the Chinese National Standards for Stationary Fire Pumps. Standard GB 6245-2006 states that, in an emergency, fire pumps must be able to achieve overload conditions and expel high flow rates of water to aid in fire extinguishing. At

1.5 times the rated flow, the pressure head must not be lower than 65% of the rated pressure. The pump is designed to be used exclusively under emergency conditions when there is a fire outbreak. In these situations, high flow rates are required. This means that the pump is mostly operated either at the design flow rate or at overload conditions. This aspect necessitated the analysis at these flow conditions.

It must be noted that the vertical fire pump under investigation was previously optimized by Zhang *et al.* (2021) to stabilize the power performance curve. The optimized model geometry was re-meshed and the setup was simulated independently with four different turbulence models, while maintaining all the other parameters constant. For the sake of this study, the original model shall be called the Ref. Model (Reference Model). The obtained results are compared with both the numerical results and the experimental results from the Reference Model for validation. This article can help in deciding which turbulence model would be most suitable to use to simulate the inner flow of a vertical fire pump.

## 2. NUMERICAL MODELING

### 2.1 Governing Equations

The Reynolds-Averaged Navier–Stokes (RANS) equations, as well as the mass conservation and turbulent viscosity models, govern the flow. The fluid flow is considered to be incompressible, turbulent, and three-dimensional for the sake of this analysis. Mass conservation equations can be written as follows:

$$\frac{\partial \rho}{\partial t} + \nabla \cdot (\rho \vec{v}) = 0 \quad (1)$$

In incompressible flow, the density of a fluid is constant and Eqn. (1) can be written as follows:

$$\nabla \cdot \vec{v} = 0 \quad (2)$$

where  $\rho$  is the density of the fluid,  $\vec{v}$  is the velocity vector of the flow,  $t$  is the time, and  $\nabla$  is the vector operator and can be expressed in the Cartesian plane as follows:

$$\nabla = i \frac{\partial}{\partial x} + j \frac{\partial}{\partial y} + k \frac{\partial}{\partial z} \quad (3)$$

This equation is the general form to solve any problem involving compressible or incompressible and steady or transient flow.

The momentum equation is expressed as follows:

$$\rho \left[ \frac{\partial \bar{u}_i}{\partial t} + \frac{\partial (\bar{u}_j \bar{u}_i)}{\partial x_j} \right] = \frac{\partial}{\partial x_j} \left[ \mu \left( \frac{\partial \bar{u}_i}{\partial x_j} \right) - \rho \overline{u'_j u'_i} \right] - \frac{\partial \bar{p}}{\partial x_i} \quad (4)$$

Here,  $\rho$  and  $\mu$  denote density and dynamic viscosity,  $u_i$  and  $u_j$  represent the time-averaged velocities,  $p$

represents the pressure, and, finally, the Reynolds stress tensor is expressed as -  $\overline{\rho u'_i u'_j}$

$$-\overline{\rho u'_i u'_j} = \mu_t \left( \frac{\partial \overline{u}_j}{\partial x_i} + \frac{\partial \overline{u}_i}{\partial x_j} \right) - \frac{2}{3} \delta_{ij} \left( \rho k + \mu_t \frac{\partial \overline{u}_k}{\partial x_k} \right) \quad (5)$$

$\delta_{ij}$  is the Kronecker delta,  $\delta_{ij} = \begin{cases} 1 & \text{for } i = j \\ 0 & \text{for } i \neq j \end{cases}$   $i, j = 1, 2, 3$

## 2.2 Turbulence Models

In this paper, four turbulence models are used for analysis. They are the RNG  $k-\epsilon$  model, standard  $k-\epsilon$  model, standard  $k-\omega$ , and lastly the Shear Stress Transport (SST)  $k-\omega$  model.

### 2.2.1 Standard $k-\epsilon$

The standard  $k-\epsilon$  turbulence model is made up of two equations, which consist of the equation for turbulent kinetic energy  $k$  and the equation for turbulent dissipation  $\epsilon$ , which are used to compute the eddy viscosity as (ANSYS 2016) follows:

$$\mu_t = C_\mu \rho \frac{k^2}{\epsilon} \quad (6)$$

### 2.2.2 RNG $k-\epsilon$

This model is obtained by performing a renormalization group analysis of the Navier–Stokes equations. The transport equations for turbulent kinetic energy and turbulence dissipation do not differ from the standard  $k-\epsilon$  model, with the exception that the model constant is substituted by a function. The ANSYS CFX-solver theory guide clearly states the details of the equations and functions (ANSYS 2016).

### 2.2.3 Standard $k-\omega$

The near-wall resolution at flows of low Reynolds number is an advantage of the standard  $k-\omega$  model. It is also more stable and precise because it has no need to rely on the complex non-linear damping functions required for the standard  $k-\epsilon$  model. Considering the work of Wilcox (1988, 1994), the  $k-\omega$  model assumes that the turbulence viscosity  $\mu_t$  is related to the turbulence kinetic energy  $k$  and turbulent frequency  $\omega$ , by the equation below (ANSYS 2016):

$$\mu_t = \rho \frac{k}{\omega} \quad (7)$$

### 2.2.4 Shear Stress Transport (SST) $k-\omega$

The shear stress transport (SST) model is a blend of two models. It consists of the standard  $k-\omega$  and  $k-\epsilon$  equations, which automatically shift from near-wall layers to free-stream flows. Menter (1993, 1994) expressed the transport equations for turbulent kinetic energy and its dissipation rate for the SST  $k-\omega$  model.

## 2.3 Three-Dimensional Pump Model

Figure 1 displays the 3D structure of the vertical fire pump. The pump is composed of four main components, namely an inlet pipe, outlet pipe,

impeller, and guide vane. It has a specific speed of 157.3, which is defined in Eq. (8).

$$n_s = \frac{3.65n\sqrt{Q_d}}{H^{0.75}} \quad (8)$$

where  $n_s$  is the non-dimensional specific speed of the pump,  $n$  (rpm) is the rotational speed of the impeller,  $Q_d$ (m<sup>3</sup>/s) is the design flow rate, and  $H$ (m) denotes the pressure head. Table 1 gives a summary of the geometric parameters of the vertical fire pump used in this study.

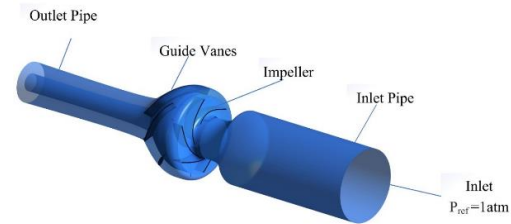


Fig. 1. 3D vertical fire pump model.

Table 1 Geometric Parameters of Vertical Fire Pump

Parameter	Data
Impeller inlet diameter	209 mm
Impeller outlet diameter	383 mm
Impeller outlet width	58.7 mm
Number of blades	6
Number of guide vanes	5
Rated flow rate	240 L/s
Rated head	43.3 m
Rotational speed	1485 r/min

## 2.4 Grid Independence Analysis

The structure of the vertical fire pump is very complex, so the generation of structured hexahedral grids was performed by using ANSYS ICEM software. In order to ensure simulation stability, the pipes at the inlet and outlet were extended to avoid reverse flow. The grids were further refined near the walls to achieve better boundary flow behavior. The mesh overview is shown in Fig. 2, and the average  $y+$  distribution on the impeller surface, shown in Fig. 3, was less than 20.

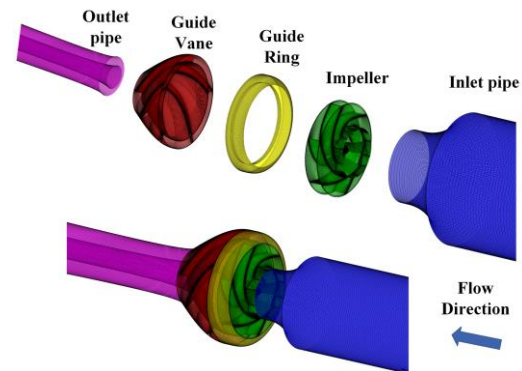
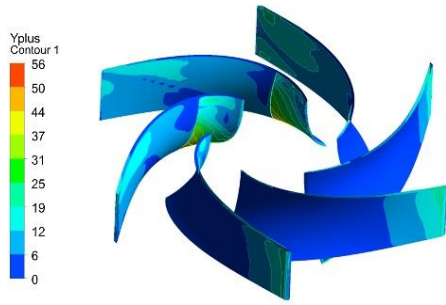
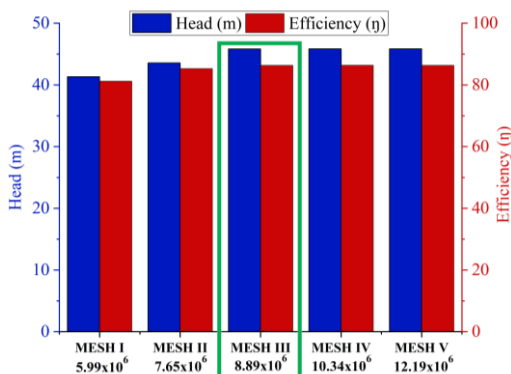


Fig. 2. Mesh overview of the flow domain.



**Fig. 3. Blade surface  $y^+$  distribution.**

Considering the work of Celik (2008), five different structured meshes with hexahedral elements were generated to conduct a grid sensitivity study. Steady state calculations were performed at  $Q_d = 240$  L/s to determine the impact of the mesh on the pressure head and efficiency of the pump. The meshes that met the design requirements of the pump (head 43.3m and efficiency 78.5%) were named III, IV, and V. When the meshes with higher grid numbers were simulated, the change in pump performance yielded 0.024% and 0.011% for head and efficiency, respectively, as shown in Fig. 4. This indicated that as the grid number increased to 8.89 million elements, there were no significant changes in numerical accuracy. Furthermore, as it has been proven that performance parameters such as the head or efficiency alone are not sufficient for grid independence (Liu *et al.* 2016; Pei *et al.* 2019; Wang *et al.* 2020), Grid Convergence Index (GCI) analysis was also conducted, where the effects of mesh density on the stability of the head values were considered. In conclusion, mesh III was finally selected to be used for subsequent simulations to reduce the computation time by lessening the calculation requirements, as shown in Table 2. This approach has been used by several researchers to analyze grid dependence in fluid machinery research (Osman *et al.* 2019; Wang *et al.* 2021; Wang *et al.* 2020).



**Fig. 4. Head and efficiency performance comparison for the independent meshes.**

### 2.5 Numerical Simulation Setup

The numerical calculations in this paper were performed in ANSYS-CFX. Four turbulence

**Table 2 Grid Convergence Index**

Test Case	Grid number ( $\times 10^6$ )	Head (m)	Grid Convergence Index (GCI) (%)
Mesh I	5.99	41.32	5.031
Mesh II	7.65	43.55	3.962
Mesh III	8.89	45.831	1.802
Mesh IV	10.34	45.842	1.776
Mesh V	12.19	45.838	1.705

models, namely both the RNG and standard  $k-\epsilon$  models, standard  $k-\omega$ , and SST  $k-\omega$ , were selected. Each turbulence model was used to run six individual cases with varying mass flow rates ranging from  $0.65Q_d$  to  $1.5Q_d$ . In terms of wall treatment, SST  $k-\omega$  and standard  $k-\omega$  employed automatic wall functions, while the RNG  $k-\epsilon$  model and standard  $k-\epsilon$  employed scalable wall functions. All other boundary conditions were kept constant. Table 3 summarizes the boundary conditions.

**Table 3 Boundary conditions**

Boundary Conditions	Settings
Turbulence models	SST $k-\omega$ , standard $k-\epsilon$ , RNG $k-\epsilon$ , and standard $k-\omega$
Interface configuration	Transient rotor–stator
Timestep	0.000112235s ( $1^\circ$ of rotation)
Total run	0.2424s (six full rotations)
Reference pressure	101325 (Pa) = 1atm
Inlet condition	Total pressure (Pa=1atm)
Outlet condition	Mass flow rate (240kg/s)
Turbulence intensity	Medium (5%) at inlet
Wall roughness	Smooth wall
Shear condition	No slip
Convergence criterion	$10^{-5}$

To determine the effects of simulation timesteps on the transient results, a timestep independence analysis was conducted, where three timesteps, each corresponding to  $1^\circ$ ,  $2^\circ$ , and  $3^\circ$  of impeller rotation, were chosen for this analysis. Figure 5 below reveals that the effects of the timestep on unsteady pressure pulsations could not be neglected; therefore, the time step 0.000112235s, which corresponds to  $1^\circ$ , was selected.

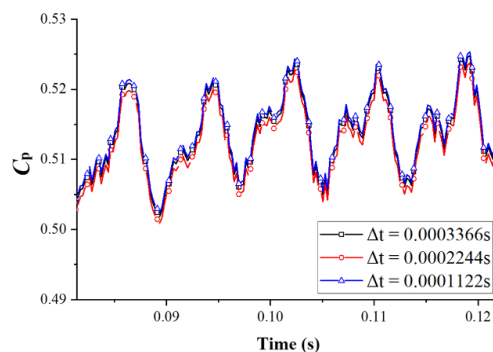


**Fig. 5. Timestep independence.**

### 3. EXPERIMENTAL MODEL AND SETUP

In determining the pump performance, evaluation was conducted with measurements from the flow rate, shaft torque, rotational speed, and the static pressure difference between suction and discharge points. The original pump, from which the optimized reference model was obtained, was tested in an open test bed system. The tests were carried out at the rated rotational speed for several operating conditions. The test was taken and repeated three times to ensure consistency. An illustration of the experimental setup is depicted in Fig. 6. WIKA S-11 pressure sensors with accuracy of  $\leq \pm 0.25\%$  were installed before and after the pump to measure the fluid pressure. A Krohne-UFM 3030 Electromagnetic flow sensor with accuracy of  $\leq \pm 0.50\%$  was also installed within the outlet pipe to monitor the fluid flow rate. The SGDN-50 torque sensor with accuracy of  $\leq \pm 0.05\%$  was installed on the pump shaft to measure the torque being produced. The accuracies of the sensors were in accordance with the ISO 9906-2012 Grade 1 standard, which allows an uncertainty limit of 1.5% for head and power measurements and 2% for flow rate determination. The performance characteristics, such as the efficiency and pressure head of the pump, were thereafter calculated by applying Eqs. (9) and (10), respectively, according to basic pump theory (Gulich 2008).

$$\eta = \frac{\rho g Q H}{P} \quad (9)$$

$$H = \frac{P_2 - P_1}{\rho g} \quad (10)$$

where  $\eta(\%)$  is the efficiency of the pump,  $\rho(\text{kg/m}^3)$  denotes the fluid density,  $g(\text{m/s}^2)$  denotes the gravitational acceleration,  $Q(\text{m}^3/\text{h})$  is the flow rate,  $H(\text{m})$  denotes the pressure head,  $P(\text{W})$  is the power, and  $P_1$  and  $P_2$  denote the inlet and outlet pressure, respectively.

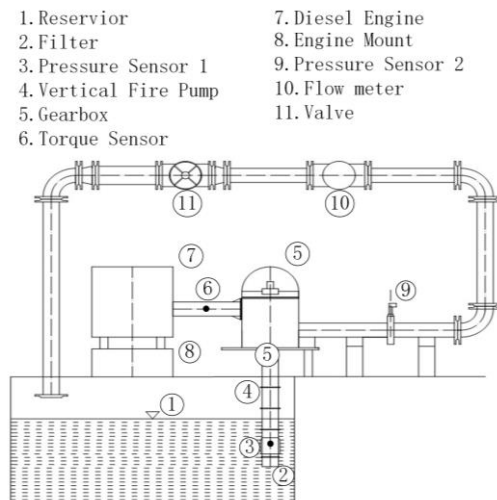


Fig. 6. Diagram of experimental setup.

### 4. DISCUSSION OF RESULTS

#### 4.1 Experimental Validation

The comparison of head, power, and efficiency performance between the simulated cases and the experiment is shown in Fig. 7. Both the Ref. Model and optimized simulated models show a significant improvement over the experimental model. It must be noted that the simulation of the Ref. Model employed the use of the RNG  $k-\epsilon$  turbulence model. This was expected as the simulated models did not account for mechanical losses in the flow.

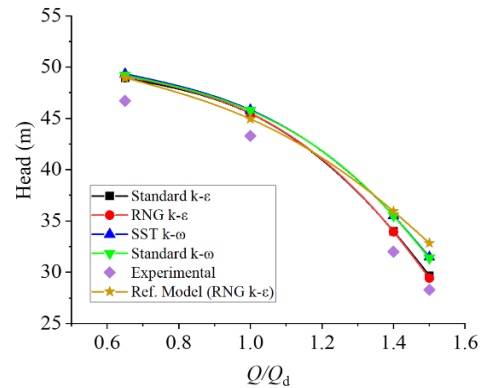


Fig. 7a. Head comparison between CFD simulations and experiment.

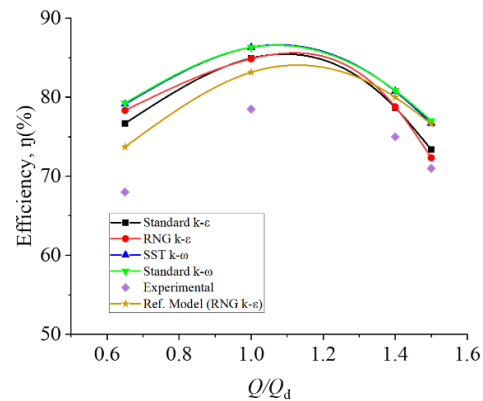


Fig. 7b. Efficiency comparison between CFD simulations and experiment.

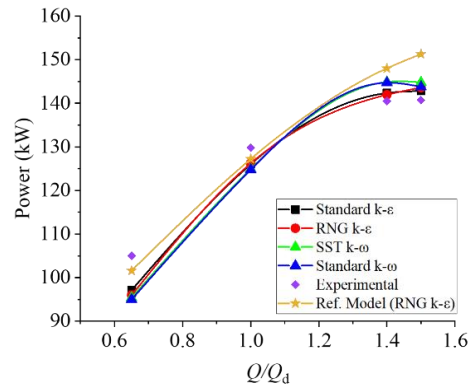


Fig. 7c. Power comparison between CFD simulations and experiment.

The pressure head characteristic curve is shown in Fig. 7a. In general, as the flow rate increased, the head for both CFD and experimental tests decreased, as expected. As the flow rate increased, the pump head decreased continuously from part-loads, design point, and overload operating conditions. The drop in head was much steeper at overload conditions. At the best efficiency point (BEP), the Ref. Model CFD and the experimental setup recorded a pressure head of 44.95m and 43.3m, respectively. This represents a 3.8% error margin, which is acceptable. In the case of the optimized model, at the BEP, the pressure head values of the various turbulence models used ranged from 45.4m to 45.8m.

Figure 7b shows that the efficiency of both the CFD and the test increased to the best efficiency point (BEP) at a flow rate of 240 L/s ( $1.0Q_d$ ) and then began to drop steadily. The hydraulic efficiency of the Ref. Model CFD and the experimental configuration was 83.15% and 78.50%, respectively, at the best efficiency point. In the case of the optimized model, the BEP of the various turbulence models used ranged from 84.8% to 86.3%.

As shown in Fig. 7c, the power curve for both the CFD and the test increased steadily as the flow rate increased and the trend continued until the overload region, where it began to normalize. At the BEP of 240 L/s ( $1.0 Q_d$ ), the Ref. Model and experimental setup recorded power usage of 127.2 kW and 129.8 kW, respectively. This represents a 1.5% error margin in power. For the optimized model and considering the turbulence models, there was no significant difference between them for all recorded flow rates.

## 4.2 CFD Models' Performance against the Experiment.

### 4.2.1 Head Performance of CFD against Experiment

Between  $0.65Q_d$  and  $1.0Q_d$ , the head gain trend was generally similar across all turbulence models; however, differences emerged after the flow increased above  $1.0Q_d$ . This is seen in Fig. 8.

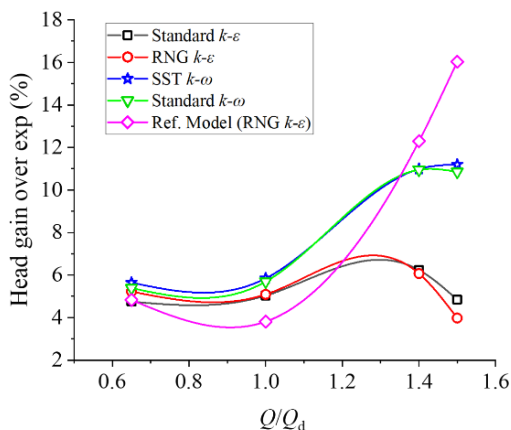


Fig. 8. Head performance of CFD over experiment.

The SST  $k-\omega$  and standard  $k-\omega$  models were able to sustain higher head than the remaining two turbulence models. They maintained an almost identical trend until  $1.5Q_d$ , where the standard  $k-\omega$  model dipped slightly below the SST  $k-\omega$ . The head values of both the RNG and standard  $k-\epsilon$  models also had an identical trend, albeit lower. Approaching  $1.5Q_d$ , the RNG  $k-\epsilon$  dipped lower than the standard  $k-\epsilon$ .

### 4.2.2 Efficiency Performance of CFD against Experiment

In Fig. 9, the efficiency gains of the CFD cases over the experimental setup are presented. At  $0.65Q_d$  through to  $1.5Q_d$ , the performance gains of the CFD models ranged from 8.4% up to 16.56%. The SST  $k-\omega$  and the standard  $k-\omega$  models followed a similar trend. From the lower range of flow rates to the design flow rate, there was a loss in efficiency gains, which continued until approximately  $1.2Q_d$ , where it began to stabilize and then started to slowly rise again at a high flow rate of  $1.4Q_d$ . The RNG  $k-\epsilon$  model lost its efficiency gains at the lower flow rates but stabilized briefly at the design flow rate, after which it dropped again within the high-flow-rate zone.

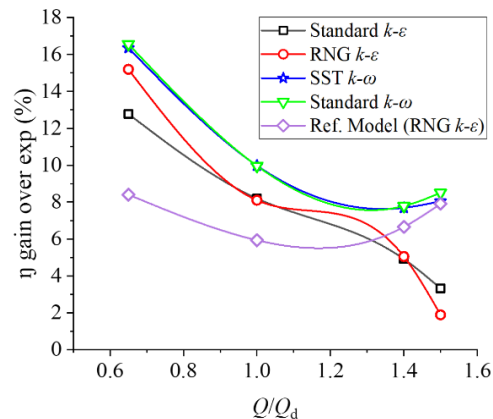


Fig. 9. Efficiency performance of CFD over experiment.

### 4.2.3 Power Performance of CFD against Experiment

Figure 10 shows a graph depicting the power saved by the CFD over the experimental value. The power input from the engine coupled to the vertical fire pump was recorded at four flow rates and plotted against the same flowrates for the Ref. Model setup and also for the optimized setup with the selected turbulence models. At  $0.65Q_d$ , the Ref. Model used approximately 3.3% less power than the experimental model, which dropped to around 2% at  $1.0Q_d$ . At  $1.4Q_d$  and  $1.5Q_d$ , the original model over-predicted the power usage by around 5% and 7%, respectively. Considering the optimized model with the different turbulence models, it can be seen that at  $0.65Q_d$ , on average, the optimized model used approximately 6.2% less power compared to the Ref. Model, and a further 9.5% less than the experimental value. At the design flow rate  $1.0Q_d$ ,

the power usage of the optimized models, on average, hovered around the value of 3.4% less, which is a significant drop from  $0.65Q_d$ . Similar to the Ref. Model, the optimized models also tended to over-predict the power use at the high-flow-rate zones, by 2.06% and 2.10% for  $1.4Q_d$  and  $1.5Q_d$ , respectively. However, it was noticed that the margin by which it over-predicted the power usage was much smaller than that of the Ref. Model.

### 4.3 Static Pressure Pattern for Optimized Model with Different Turbulence Models

Figure 11 shows the pressure pattern in the impeller region of the optimized model, obtained at the impeller midspan, for  $1.0Q_d$  and  $1.5Q_d$  flow rates and their corresponding turbulence models. The flow structure in the impeller midspan of the pump varied as the flow rate changed. The results revealed that when the pump ran at flow rates higher than  $1.0Q_d$ , the low-pressure area at the impeller's inlet region expanded and propagated into the flow channels, and then the pressure increased as it moved further along the channel. At the outlet, the pressure was higher under  $1.0Q_d$  than at  $1.5Q_d$ . This increase in pressure in the radial direction is characteristic of centrifugal pumps, and the drop in pressure as the flow rate increases is evident in the performance graphs.

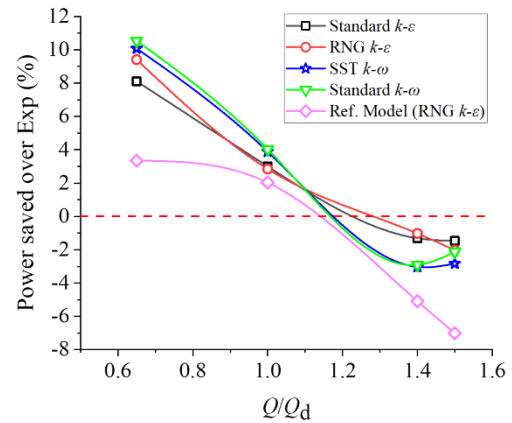


Fig. 10. Power performance of CFD over experiment.

Figure 13 shows the pressure patterns in the guide vane flow channels of the optimized model. The pressure contours were obtained at different planes, as indicated in Fig. 12. The planes named 0.1, 0.5, and 0.9 span represent the planes at the inlet, middle section, and outlet section of the guide vane, respectively. These planes have been stacked atop each other to create a concentric image of all the

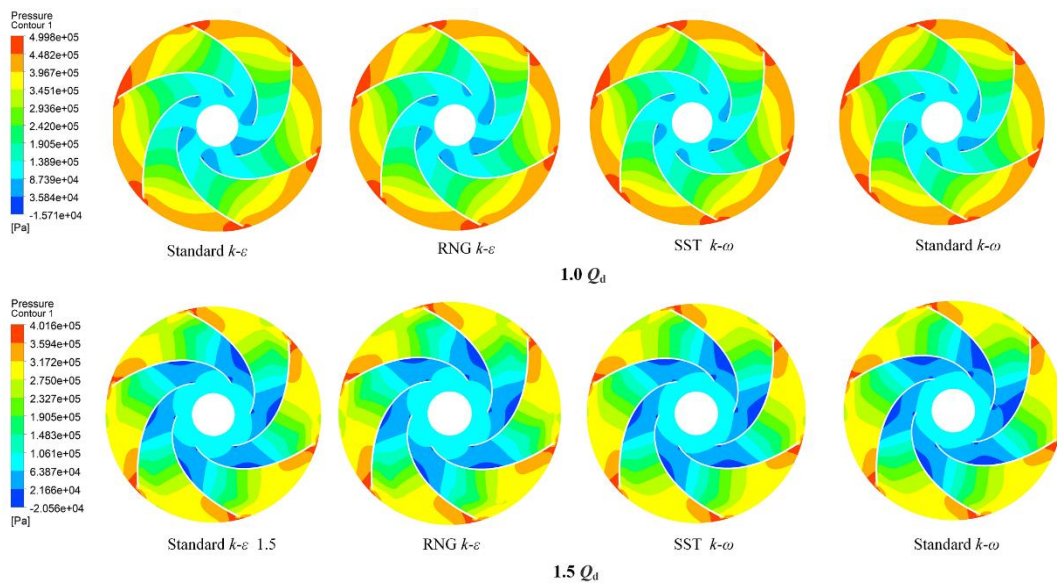


Fig. 11. Pressure distribution at impeller midspan.

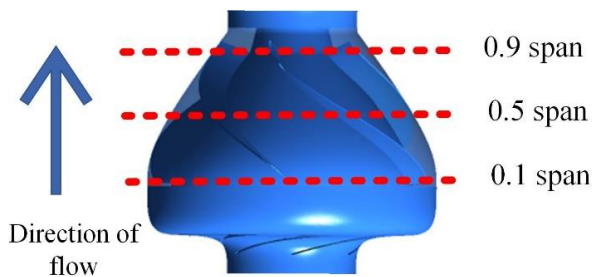
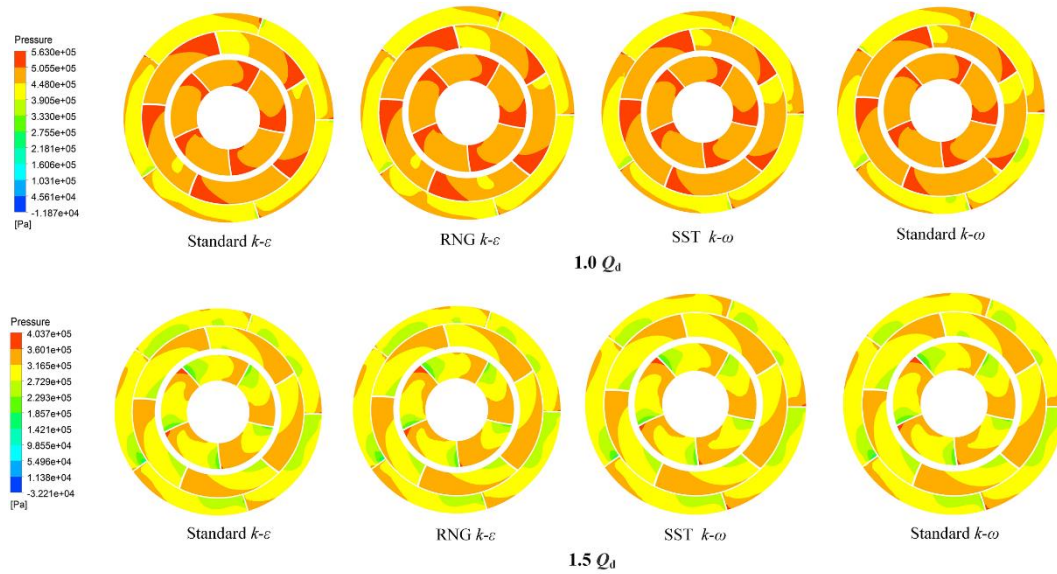
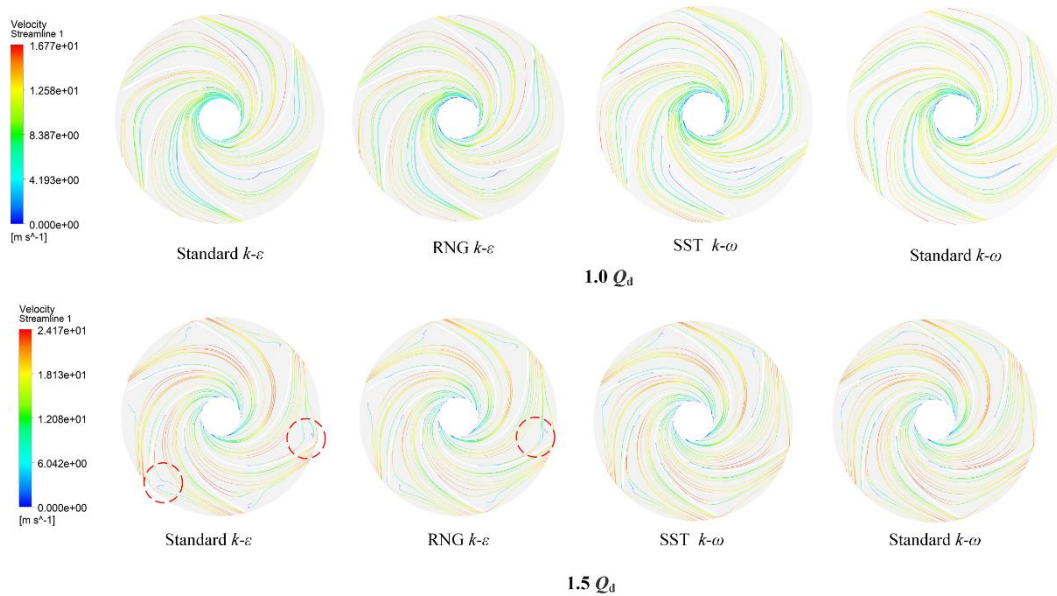


Fig. 12. Locations of cut planes for pressure analysis in guide vane.



**Fig. 13. Pressure distribution in guide vane flow channel.**



**Fig. 14. Velocity streamline distribution at impeller midspan.**

planes from a top view. All of the pressure contours across the different flow rates shown in the analysis figure have been illustrated on the same scale for fair comparison. It can be generally observed that the pressure reduces as the flow rates increase, and the turbulence models all show similar behavior in this regard. It can also be seen, considering the cut planes, that the pressure increases from the 0.1 span up towards 0.9 span. This can be attributed to the fact that there is a steady pressure build-up as the flow moves from the impeller and up through the guide vane. At  $1.0Q_d$  and  $1.5Q_d$ , the pressure distribution is relatively similar across all the planes and over the turbulence models. The main difference is evident in the intensity of the pressure, where the pressure value of  $1.0Q_d$  is considerably higher than that of the  $1.5Q_d$  condition.

#### 4.4 Flow Velocity Streamline Pattern for Optimized Model with Different Turbulence Models

Figure 14 shows the velocity streamline pattern in the impeller region of the optimized model, obtained at the impeller midspan, with a design load at  $1.0Q_d$  and overload at  $1.5Q_d$  of pump-rated flow, and their corresponding turbulence models. The velocity streamlines were generally uninterrupted along the passageways for the design and high flow rates. The streamlines at the design conditions were slightly smooth and uniform across all turbulence models. The streamlines at overload conditions were also orderly within the inlet and the mid-section of the flow channel. However, approaching the outlet of the flow channel near the blade tips, the extra turbulent flow at this high flow rate

created recirculation zones at the suction side of the blade tips, leading to severe energy loss and secondary flow. The velocity vector diagram in Fig. 15 clearly depicts this phenomenon. Considering the individual turbulence models in all these flow conditions, it was noted that the smallest flow irregularities could be observed in the SST  $k-\omega$  and standard  $k-\omega$  models. This behavior is reflected in the efficiency characteristics of the pump obtained earlier, presented in Fig. 7b.

Figure 16 shows the velocity streamline distributions in the guide vane region of the optimized model, obtained at the blade midspan. All of the velocity streamline contours across different

flow rates and turbulence models shown in this image are illustrated on a similar scale for fair comparison. At  $1.0Q_d$ , the recirculation formation was reduced significantly and was still confined to the suction side of the blades and nearer to the outlet. All the turbulence models predicted similar streamline formations under this condition. At  $1.5Q_d$ , the overall flow pattern was better than at other conditions, and no recirculation appeared within the flow domain of the guide vane. It must be noted, however, that under this condition, at the inlet of the guide vane, there were less vortical areas within the SST  $k-\omega$  and standard  $k-\omega$  models as compared to the others.

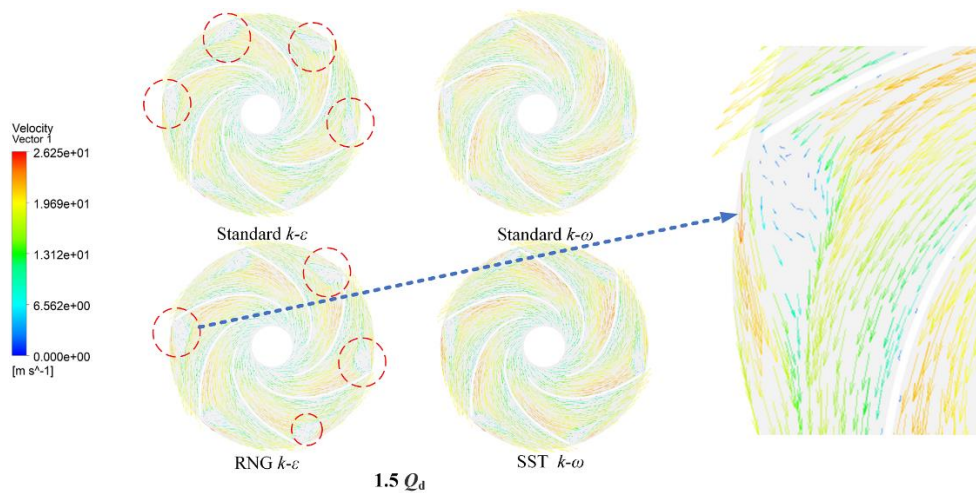


Fig. 15. Velocity vector diagram depicting recirculation zones.

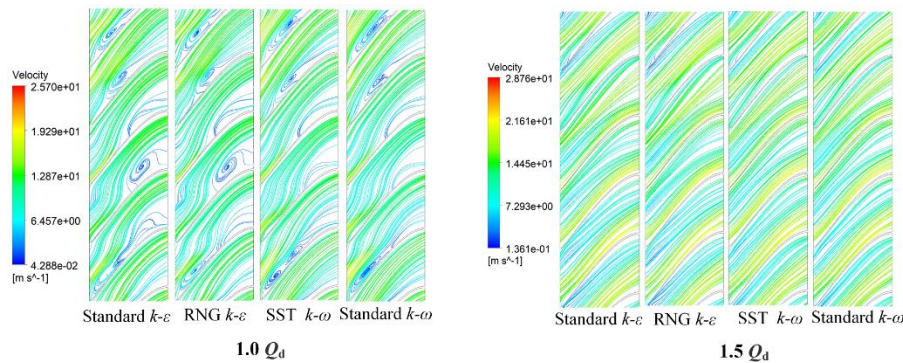


Fig. 16. Velocity streamline distribution at guide vane midspan.

#### 4.5 Turbulent Kinetic Energy Pattern for Optimized Model with Different Turbulence Models

Looking at the turbulent kinetic energy (TKE) contours, it can be observed in Fig. 17 that the turbulent kinetic energy was concentrated as a trail on the blade tips. This depicts the wake that is left behind as the blade passes. It was interesting to observe that the RNG  $k-\epsilon$  produced much less TKE at the trail of the blade tips as compared to the others. This is shown in the velocity vector diagrams in Fig. 15 as recirculation zones, and it is the major cause of losses in the overload region. At the design point, it is very interesting to observe

that the SST  $k-\omega$  and the standard  $k-\omega$  turbulence models were able to resolve significantly more details in the flow channel. The turbulence kinetic energy was much more uniformly distributed within the flow channels compared to the  $k-\epsilon$  models. The SST  $k-\omega$ , however, clearly highlighted the turbulent energy areas within the flow channels, both in the free stream and also along the blade walls.

This is because the SST  $k-\omega$  model is a hybrid model that combines the desired aspects of both the  $k-\epsilon$  and  $k-\omega$  models, utilizing a smooth function to mix between flow in the near-wall region and that of the free stream. The  $k-\omega$  model handles the near-wall region while the  $k-\epsilon$  handles the free stream.

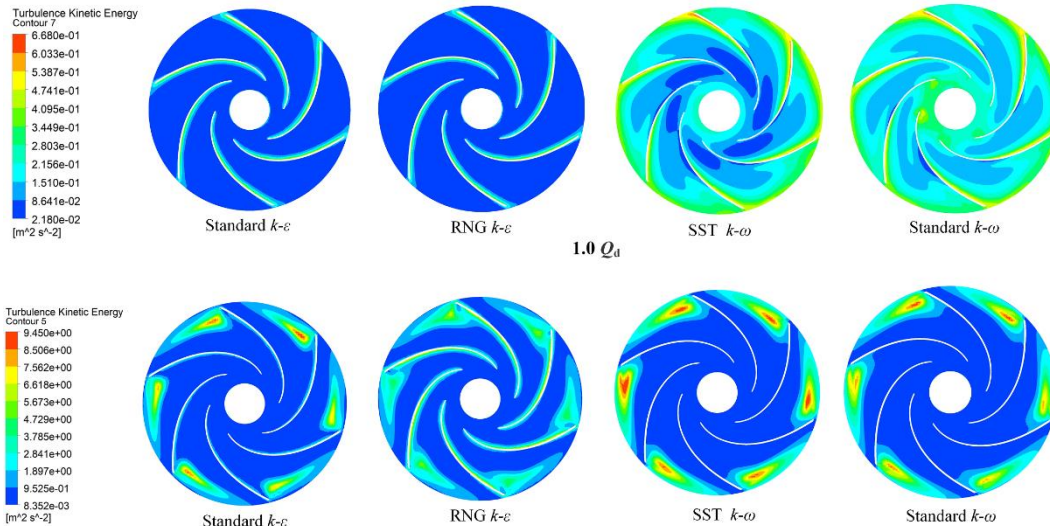


**Fig. 17. Turbulence kinetic energy distribution at impeller midspan**

Figure 18 shows the turbulence kinetic energy distributions in the guide vane region of the optimized model, obtained at the blade midspan. As the flow leaves the impeller region in a swirling motion, it makes contact with the guide vane blades. The blades are designed to receive the turbulent swirling flow from the impeller and direct it along the blades to create a more streamlined flow. This phenomenon can be seen from the turbulent kinetic energy distributions as the flow somewhat normalizes and the turbulent kinetic energy is reduced at the outlet. This is similar across all flow rates and for all turbulence models. At the design flow rate, the areas of turbulence begin to narrow and confine themselves to the suction side of the blades. It is also noticed that the general level of turbulence kinetic energy is significantly reduced. At  $1.5Q_d$ , the increase in flow rate improves the flow pattern and eliminates most of the turbulence energy within the flow, except for the initial disruption that is caused by the impact of the fluid on the blades as it enters the guide vane. Overall, it is seen that the guide vane is the cause of major flow irregularities, which translate into losses and must be addressed.

## 5. UNSTEADY PRESSURE FLUCTUATION ANALYSIS

To properly track the stability of the pumps, monitoring points were placed within areas of interest in the pump. These areas were the impeller flow channels and the guide vane flow channels. The monitoring points recorded precise minute pressure fluctuations during the operation of the pump; however, the ratio of the pressure fluctuations at the monitoring points to the absolute value of the pressure value at this point was very small; therefore, the dimensionless pressure coefficient  $C_p$  was introduced to make the observation of the pressure value at each monitoring point more appreciable. The formula for  $C_p$  calculation is shown in Eq. (11).

$$C_p = (p_i - \bar{p}) / (0.5\rho u_2^2) \quad (11)$$

where  $p_i$  (Pa) denotes the instantaneous pressure of the monitoring point,  $\bar{p}$  (Pa) is the mean value of the sum of pressure information recorded at the monitoring point,  $u_2$  (m/s) is the outlet circumferential velocity of the blade, and  $\rho$  ( $\text{kg/m}^3$ ) is the density of fluid. The recorded pressure pulsation data were processed using the Fast Fourier Transform (FFT) into the time domain and frequency domain. The pressure pulsation coefficient ( $C_p$ ) was plotted at the design point ( $1.0Q_d$ ) and overload flow conditions ( $1.5Q_d$ ) at the aforementioned monitoring points.

Figure 19 depicts the locations of the monitoring points within the computational domain of the pump. IMP represents monitors installed in the flow channels of the impeller and GV represents points within the flow channels of the guide vane.

### 5.1 Time Domain Analysis of Pressure Pulsations.

The plotted graphs represent variations in  $C_p$  with respect to a time range of 0.0407s, which represents one complete rotation period of the impeller. Figure 20 depicts the time domain history of  $C_p$  at  $1.0Q_d$  and  $1.5Q_d$  in the impeller flow passages of the pump. IMP1 represents the impellers in the stages of the pump. The attached letters A-F refer to the six flow channels within the impeller. At  $1.0Q_d$ , for all stages, the graph depicts five peaks and five valleys, which correspond to the number of blades in the guide vane. This is an obvious depiction of the rotor–stator influence as the stationary guide vane and the rotating impeller affect the pressure pulsations within the impeller. Considering the trends of the pulsations, it is seen that the amplitudes of the  $C_p$  values increased as the flow rates increased.

Figure 21 depicts the time domain history of the pressure fluctuation coefficient within the guide vanes at both flow rates. The guide vane of this

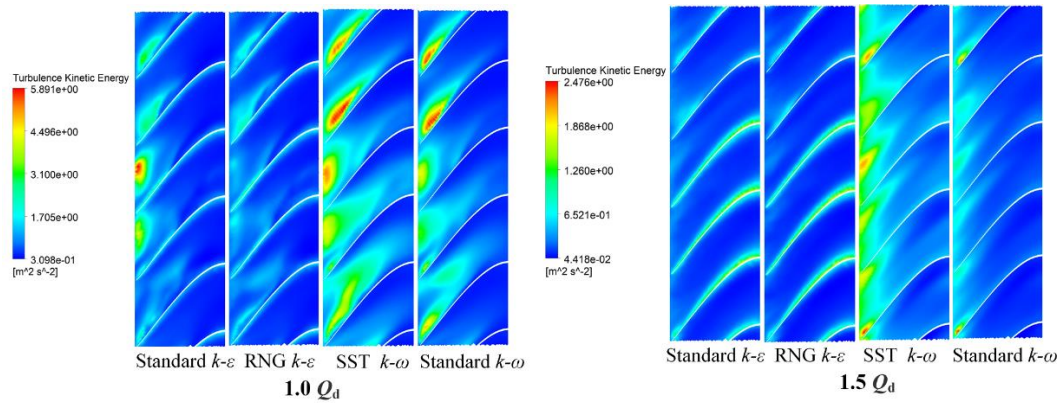


Fig. 18. Turbulence kinetic energy distribution at guide vane midspan.

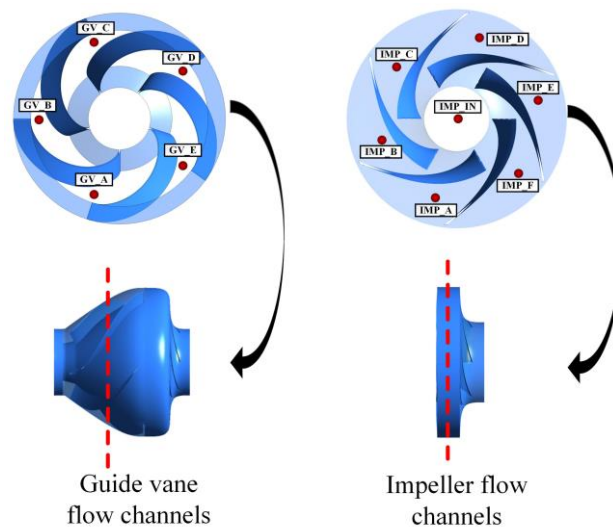


Fig. 19. Locations of monitoring points.

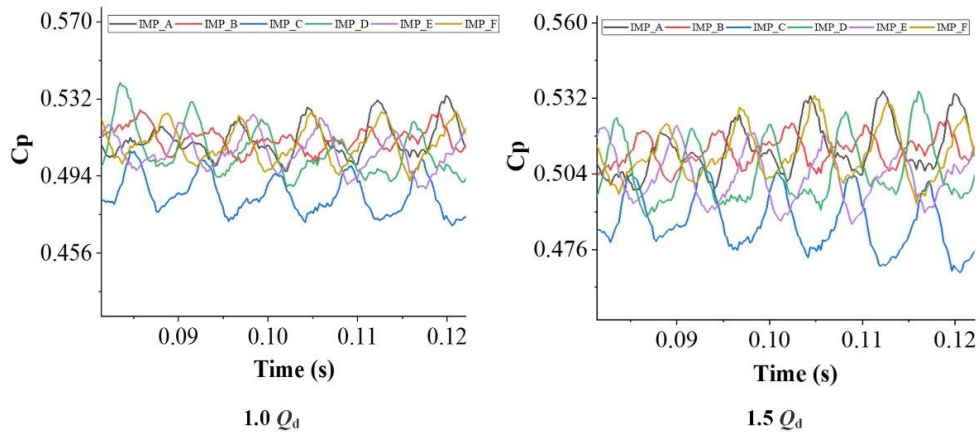


Fig. 20. Time domain history of  $C_p$  fluctuations on impeller flow channels

pump is the point where most of the swirling flow from the impeller is channeled axially and then diffused to increase the overall head. All the monitoring points recorded fluctuations that had periodicity and clearly depicted six peaks. This corresponds to the number of impeller blades. The amplitudes of the pulsations within the guide vane

were very similar at both the design and overload flow conditions.

## 5.2 Frequency Domain Analysis of Pressure Pulsations

Figure 22 shows the frequency domain plot for the  $C_p$  values within the impeller flow passages. With

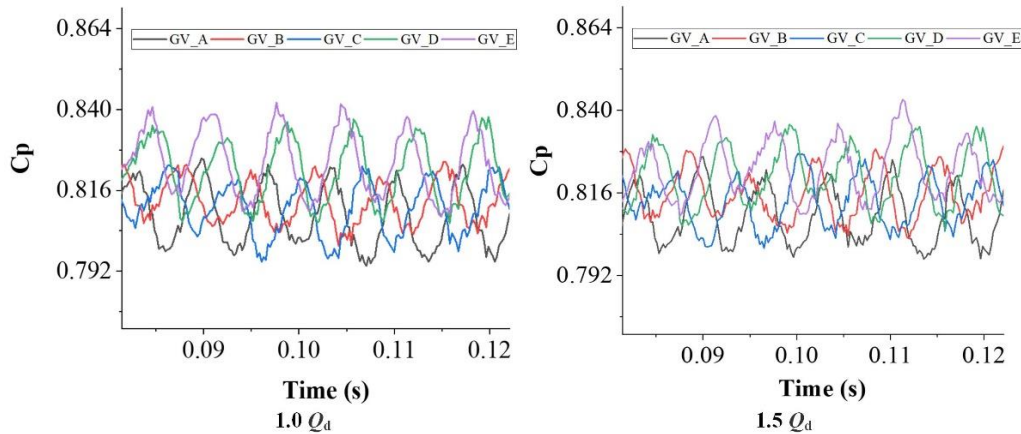


Fig. 21. Time domain history of  $C_p$  fluctuations in guide vane

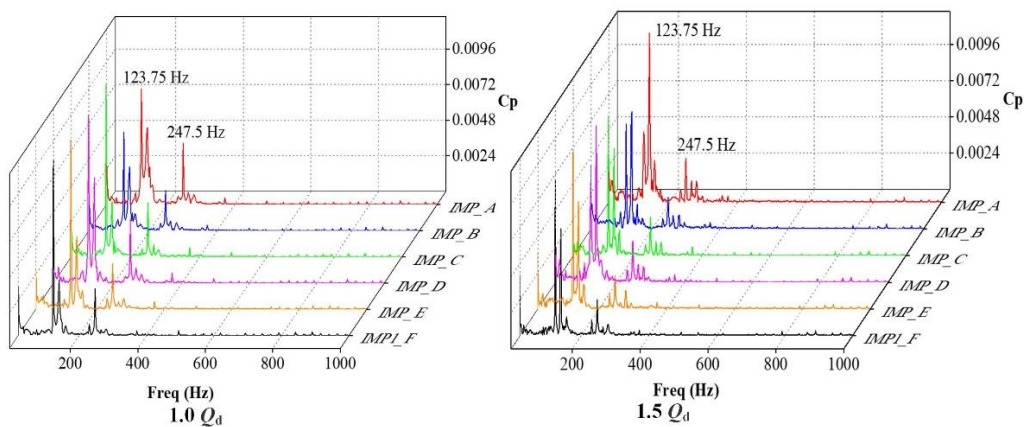


Fig. 22. Frequency domain history of  $C_p$  fluctuations in impeller flow channels.

the impeller rotational speed at 1485 r/min, the shaft frequency  $f_n$  occurs at 24.75 Hz. Due to the six blades of the impeller and five blades of the guide vane, the blade passing frequencies (BPF) of these components are  $6f_n$  and  $5f_n$ , respectively. It was observed that for both design and overload flow conditions, the main excitation frequency within the impeller flow channels occurred at 123.75 Hz ( $5f_n$ ), with the 2<sup>nd</sup> harmonic of BPF occurring at ( $10f_n$ ). This shows the influence of the guide vane blades on pulsations within the impeller.

In the guide vane, the frequencies excited by pressure fluctuations occurred at BPF of 148.5 Hz ( $6f_n$ ), while the 2<sup>nd</sup> harmonic of BPF occurred at 297 Hz ( $12f_n$ ), as seen in Fig. 23. It was also observed that under overload flow conditions, there appeared to be an influence of pulsations that do not occur at the shaft frequency or any of its harmonics, but still present significant amplitudes. This occurrence can be attributed to the increased pulsations that occur within the pump while it operates in overloaded and relatively unstable conditions.

## 6. CONCLUSIONS

In this study, the effects of various turbulence models on a vertical fire pump were explored using

CFD simulations. The flow domains in the rotating impeller and guide vane, together with the pump performance, were analyzed and compared with experimental results. The analysis of the results revealed the following:

(1) CFD largely has the ability to predict the steady flow in the impeller region of a pump, and the CFD results showed good agreement with experimental values, with minimal disparity. The CFD models had a higher head and efficiency compared to the measured values of 5.41% and 9.03% for head and efficiency, respectively. This was expected, as mechanical losses were not accounted for in the simulations. Moreover, comparing the performance of the CFD models according to the turbulence models used, it was revealed that, on average, the SST  $k-\omega$  model showed 1.82% and 0.81% improvements in efficiency and head, respectively, over the  $k-\epsilon$  models. In terms of the power performance, however, standard  $k-\epsilon$  is less likely to over-predict the power used by the pump in overload conditions as compared to the other turbulence models.

(2) For the pressure and velocity fields, the static pressure values and velocity values did not show significant reactions to the turbulence models. As expected, pressure at the midspan of the pump rises radially from the impeller eye towards the impeller

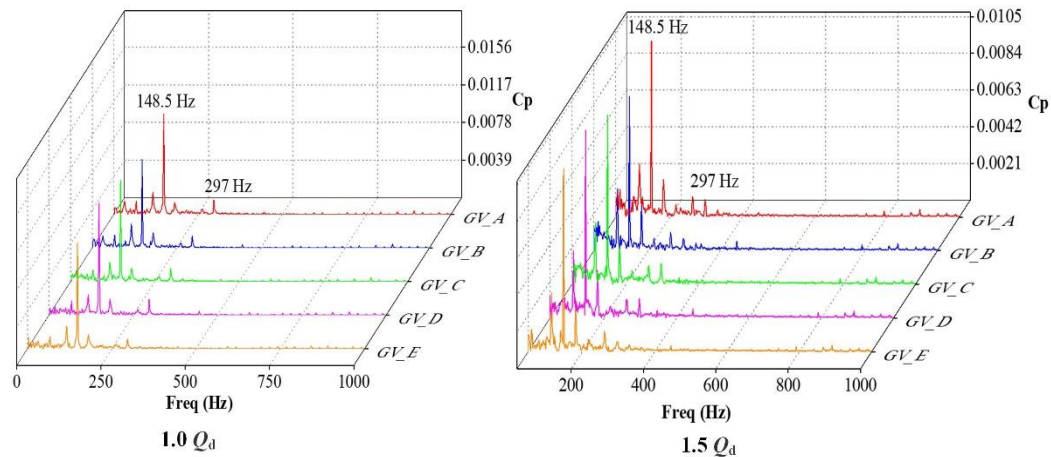


**Fig. 23. Frequency domain history of  $C_p$  fluctuations in guide vane.**

outlet. With regard to the different turbulent models, the variation in pressure was comparable for all.

(3) For the velocity streamlines, at a low flow rate, there were significant areas of flow separation and recirculation zones for every turbulence model used. Both the RNG  $k-\varepsilon$  and standard  $k-\varepsilon$  showed fewer of these areas compared to the others. At the design operating point, no flow separations were detected in most of the flow channel until approaching the outlet, where small areas of separation were noticed. At a high flow rate, again, there were no flow separations observed in the main flow channel; however, at the impeller outlet, pockets of extra turbulent flow created recirculation zones at the suction side of the blade tips. This may lead to severe energy losses.

(4) SST  $k-\omega$  was the best-performing turbulence model in terms of head and efficiency, and this was evident in both the performance curves and the experimental results presented in similar works in the literature. Moreover, it was able to resolve more details in the turbulence kinetic energy contours. However, in terms of the power performance, RNG  $k-\varepsilon$  and standard  $k-\varepsilon$  performed best in overload conditions. In this case, even though RNG  $k-\varepsilon$  and standard  $k-\varepsilon$  have their advantages, SST  $k-\omega$  is the ideal turbulence model for use.

(5) The pressure fluctuation analysis revealed that within the impeller domain, the frequencies excited by pressure fluctuations occurred at 123.75 Hz ( $5 \times f_n$ ), 247.5 Hz ( $10 \times f_n$ ), and 371.25 Hz ( $15 \times f_n$ ), with the major influence coming from the number of blades of the guide vane, while, within the guide vane, the excitation frequencies occurred at 148.5 Hz ( $6 \times f_n$ ) and 297 Hz ( $12 \times f_n$ ) due to the influence of the impeller blades.

#### ACKNOWLEDGEMENTS

This work was supported by the Primary Research & Development Plan of Jiangsu Province (Grant no. BE2019009-1). The authors declare no competing financial interests.

#### REFERENCES

- Al-Obaidi, A. R. (2019). Effects of different turbulence models on three-dimensional unsteady cavitating flows in the centrifugal pump and performance prediction. *International Journal of Nonlinear Sciences and Numerical Simulation* 20(3-4), 487-509.
- ANSYS, C. F. X. (2016). Version 17.0, ANSYS CFX-solver theory guide. *Canonsburg, PA: Ansys Inc.*
- Asuaje, M., F. Bakir, S. Kouidri, F. Kenyery and R. Rey (2005). Numerical modelization of the flow in centrifugal pump: volute influence in velocity and pressure fields. *International Journal of Rotating Machinery* 2005(3), 244-255.
- Celik, I. B., U. Ghia, P. J. Roache and C. J. Freitas (2008). Procedure for Estimation and Reporting of Uncertainty Due to Discretization in CFD Applications. *Journal of Fluids Engineering* 130(7), 078001.
- Chalghoum, I., H. Kanfoudi, S. Elaoud, M. Akroud and R. Zgolli (2016). Numerical modeling of the flow inside a centrifugal pump: Influence of impeller-volute interaction on velocity and pressure fields. *Arabian Journal for Science and Engineering* 41(11), 4463-4476.
- Deniz, S., A. Del Rio and E. Casartelli (2019). Experimental and numerical investigation of the speed-no-load instability of a low specific speed pump-turbine with focus on the influence of turbulence models. *IOP Conference Series: Earth and Environmental Science* 240(8), 82005.
- Feng, J., F. K. Benra and H. J. Dohmen (2010). Application of different turbulence models in unsteady flow simulations of a radial diffuser pump. *Forschung Im Ingenieurwesen* 74(3), 123-133.
- Gulich, J. F. (2008). *Centrifugal Pumps*, Springer. Berlin, Germany.

- Hu, B., S. Yuan, W. Lu, T. Li and C. Guo (2012). Numerical optimal design of a non-overload centrifugal pump. *Fluids Engineering Division Summer Meeting* 44755, 427–433.
- Joshi, J. B., N. K. Nere, C. V. Rane, B. N. Murthy, C. S. Mathpati, A. W. Patwardhan and V. V. Ranade (2011). CFD simulation of stirred tanks: Comparison of turbulence models (Part II: Axial flow impellers, multiple impellers and multiphase dispersions). *The Canadian Journal of Chemical Engineering* 89(4), 754–816.
- Koranteng, O., M., W. Wang, J. Yuan, J. Zhao, Y. Wang and J. Liu (2019). Flow loss analysis of a two-stage axially split centrifugal pump with double inlet under different channel designs. *Proceedings of the Institution of Mechanical Engineers, Part C: Journal of Mechanical Engineering Science* 233(15), 5316–5328.
- Liu, X., Y. Luo, and Z. Wang (2016). A review on fatigue damage mechanism in hydro turbines. In *Renewable and Sustainable Energy Reviews* (Vol. 54).
- Menter, F. (1993). Zonal two equation k-omega turbulence models for aerodynamic flows. *23rd Fluid Dynamics, Plasmadynamics, and Lasers Conference*, 2906.
- Menter, F. R. and Y. Egorov (2010). The scale-adaptive simulation method for unsteady turbulent flow predictions. Part 1: theory and model description. *Flow, Turbulence and Combustion* 85(1), 113–138.
- Menter, F. R. and Y. Egorov (2006). Revisiting the turbulent scale equation. *IUTAM Symposium on One Hundred Years of Boundary Layer Research*, 279–290.
- Menter, F. R. (1992). Influence of freestream values on k-omega turbulence model predictions. *AIAA Journal* 30(6), 1657–1659.
- Menter, F. R. (1994). Two-equation eddy-viscosity turbulence models for engineering applications. *AIAA Journal* 32(8), 1598–1605.
- Menter, F. R. (2009). Review of the shear-stress transport turbulence model experience from an industrial perspective. *International Journal of Computational Fluid Dynamics* 23(4), 305–316.
- Nikou, M. R. K. and M. R. Ehsani (2008). Turbulence models application on CFD simulation of hydrodynamics, heat and mass transfer in a structured packing. *International Communications in Heat and Mass Transfer* 35(9), 1211–1219.
- Opoku, F., M. Atkinson and M. N. Uddin (2020). Numerical Investigation of an Offshore Oscillating Water Column. *American Journal of Mechanical Engineering* 8(3), 88–105.
- Pei, J., F. Zhang, D. Appiah, B. Hu, S. Yuan, K. Chen and S. N. Asomani (2019). Performance prediction based on effects of wrapping angle of a side channel pump. *Energies* 12(1), 139.
- Uddin, M. N., M. Atkinson and F. Opoku (2020). A Computational Fluid Dynamics Investigation of a Numerically Simulated Wave Tank. *American Journal of Mechanical Engineering* 8(1), 40–49.
- Wang, M., Y. Li, J. Yuan and F. K. Osman (2021). Matching optimization of a mixed flow pump impeller and diffuser based on the inverse design method. *Processes* 9(2).
- Wang, W., M. K. Osman, J. Pei, S. Yuan, J. Cao and F. K. Osman (2020). Efficiency-House Optimization to Widen the Operation Range of the Double-Suction Centrifugal Pump. *Complexity*, 2020.
- Wilcox, D. C. (1988). Reassessment of the scale-determining equation for advanced turbulence models. *AIAA Journal* 26(11), 1299–1310.
- Wilcox, D. C. (1994). Simulation of transition with a two-equation turbulence model. *AIAA Journal* 32(2), 247–255.
- Yu, K. (2014). Analysis of the characteristics of vertical long-axis fire pumps. *First National Conference on Fire Protection of Supertall Buildings* 01(01), 1–18.
- Zhang, J., D. Appiah, F. Zhang, S. Yuan, Y. Gu and S. N. Asomani (2019). Experimental and numerical investigations on pressure pulsation in a pump mode operation of a pump as turbine. *Energy Science & Engineering* 7(4), 1264–1279.
- Zhang, J., Z. Yang, L. Lai, H. Song and C. Jing (2021). Automatic Optimization of Vertical Long-shaft Fire Pump Overload Based on Particle Swarm Optimization Algorithm. *IOP Conference Series: Materials Science and Engineering* 1081(1), 12017.